

Enhancement of the Curie temperature in $\text{NdBaCo}_2\text{O}_{5.5}$ by A-site Ca substitution

S. Kolesnik,^{1,*} B. Dabrowski,^{1,2} O. Chmaissem,^{1,2} S. Avci,² J. P. Hodges,³ M. Avdeev,⁴ and K. Świerczek^{1,2,5}

¹Physics Department, Northern Illinois University, DeKalb, Illinois 60115, USA

²Materials Science Division, Argonne National Laboratory, Argonne, Illinois 60439, USA

³Spallation Neutron Source, Oak Ridge National Laboratory, Oak Ridge Tennessee 37831, USA

⁴Bragg Institute, Australian Nuclear Science and Technology Organization, Menai, New South Wales 2234, Australia

⁵AGH University of Science and Technology, Faculty of Energy and Fuels, Department of Hydrogen Energy, al. A. Mickiewicza 30, 30-059 Kraków, Poland

(Received 4 June 2012; published 24 August 2012)

Layered cobaltites $\text{R}\text{BaCo}_2\text{O}_{5.5}$ (R = rare earth and Y) undergo a sequence of magnetic and electronic transitions between antiferromagnetic/ferrimagnetic/paramagnetic and insulating/paramagnetic metallic states with respective transition temperatures T_N (~ 230 – 260 K) $<$ T_C (~ 250 – 290 K) $<$ T_{MI} (~ 360 K). We have synthesized a $\text{Nd}_{1-x}\text{Ca}_x\text{BaCo}_2\text{O}_{5.5}$ series ($0 \leq x \leq 0.2$) of cation-[(Nd,Ca)/Ba]-ordered and oxygen vacancy-ordered materials and investigated them by neutron diffraction, magnetization, and electronic and thermal transport. We observe that upon Ca doping, T_N is decreasing to 0 for $x = 0.1$ and T_C is increasing and coincides with T_{MI} for $x > 0.12$, which weakly changes with Ca substitution from ~ 360 to ~ 340 K. This is the largest enhancement of T_C observed for these cobaltites. Unlike hole doping by adding oxygen, Ca doping does not disrupt the cation and oxygen vacancy orderings up to $x = 0.20$.

DOI: [10.1103/PhysRevB.86.064434](https://doi.org/10.1103/PhysRevB.86.064434)

PACS number(s): 75.30.Kz, 61.05.F–, 75.50.Gg, 72.20.Pa

I. INTRODUCTION

Layered cobaltites $\text{R}\text{BaCo}_2\text{O}_{5+\delta}$ (R = rare earth and Y) have been studied over the last several years due to interesting magnetic and electronic properties resulting from the R/Ba cation ordering along the c axis, in addition to several kinds of oxygen vacancy orderings, which depend on oxygen content.^{1–15} The oxygen content can be changed over a range from $5 + \delta = 5.0$ to 5.8 ,⁶ which changes the ground states of these materials from the charge-ordered antiferromagnetic (AFM) insulator for $\delta = 0$, to the optimally doped band insulator for $\delta = 0.5$, and finally to the heavily hole-doped metallic ferromagnetic (FM) state for $\delta > 0.7$. The particular doping level $\delta = 0.5$ is associated with an oxygen vacancy ordering, which manifests itself as alternating planes of CoO_6 octahedra and CoO_5 square pyramids along the a axis of the crystal structure, each containing one Co^{3+} ion. These optimally doped $\text{R}\text{BaCo}_2\text{O}_{5.5}$ compositions demonstrate a variety of unique temperature-dependent physical phenomena, such as a dramatic change of electronic properties (the Seebeck coefficient), a metal–insulator transition (MIT) at T_{MI} (~ 360 K), the Co^{3+} spin state transition, Co^{3+} spin state ordering at low temperatures, ferrimagnetism below T_C (~ 250 – 290 K) and antiferromagnetism below T_N (~ 230 – 260 K) $<$ T_C . In a seminal paper, Taskin *et al.* observed that these properties strongly depend on even slight oxygen nonstoichiometry.⁶ Complex properties have been associated with the varying spin state of the cobalt, which often behaves in unpredictable ways depending on the chemical composition of the investigated material and the specificity of the Co local environment.⁶ Thus, consideration of Co^{3+} and Co^{4+} ions with high spin (HS), intermediate spin (IS), and low spin (LS) states is frequently required to explain the observed behavior; however, these spin states offer an additional degree of freedom when designing new materials with tunable properties. Recent studies also suggest that assignment of a unique charge state to Co based on the chemical formula may not be possible, introducing an additional complication.⁷ $\text{R}\text{BaCo}_2\text{O}_{5+\delta}$ is one

of the most fascinating cobaltite systems because it offers several possibilities for diverse chemical substitutions at the distinct R , Ba, and Co sites, in addition to varying oxygen content. The substituting ions may have various sizes and oxidation states and therefore would act as a control parameter for modifying structural distortions and injecting or removing charges from the system without severely changing the local oxygen environment around the Co ions.

While there are several studies of the $\text{R}\text{BaCo}_2\text{O}_{5+\delta}$ compounds with variable oxygen content causing conversion of the CoO_5 pyramids to CoO_6 octahedra for $\delta > 0.5$ (or vice versa, for $\delta < 0.5$), information about the cation substitutions in these materials with controlled oxygen content is scarce. Isovalent Ca substitution for Ba destroys the AFM long-range order and stabilizes the ferrimagnetic state.¹⁶ Substitution of Ni for Co in $\text{GdBaCo}_{2-x}\text{Ni}_x\text{O}_{5+\delta}$ strongly suppresses all transition temperatures,¹⁷ while Fe substitution leads to phase separation of $\text{GdBaCo}_2\text{O}_{5.5+\delta}$ into Fe-rich and Fe-free regions.¹⁸

A particular case of substitution of heterovalent Ca for R is especially interesting, because although its effect on the crystal lattice of $\text{R}_{1-x}\text{Ca}_x\text{BaCo}_2\text{O}_{5+\delta}$ is small due to the similar ionic sizes of R and Ca, it affects the magnetic properties in various ways depending on the size of R . The substitution for a smaller-size $R = \text{Dy}$ and Ho causes large deterioration of long-range magnetic ordering in the system, ultimately leading to a paramagnetic (PM) state for $x \geq 0.2$.¹⁹ The substitution for intermediate-size europium expands drastically the range of the ferrimagnetic phase down to 10 K and increases T_C up to 320 K, but it does not affect the MIT temperature.²⁰ For other intermediate-size R ions (Y, Gd, and Sm), similar behavior is observed, indicating a correlation of T_C to the ionic size of R .²¹ All these Ca-substituted materials were synthesized in air; therefore, their oxygen content could possibly be noticeably different from 5.5, which may contribute to the observed phenomena.

In this work, we describe the structural, transport, and magnetic properties of the nearly stoichiometric system

$\text{Nd}_{1-x}\text{Ca}_x\text{BaCo}_2\text{O}_{5.5}$ with $0 \leq x \leq 0.2$. We show enhanced ferrimagnetism and preservation of the MIT in the entire substitution range. Also, it is observed that hole doping by the substitution of Ca^{2+} for R^{3+} when pyramidal and octahedral coordination is preserved leads to different effects than hole doping by excess oxygen in $\text{GdBaCo}_2\text{O}_{5+\delta}$, which changes the Co coordination to oxygen.⁶ With substitution of Ca^{2+} , a wider range of homogenous charge doped samples has been achieved than with oxygen doping, showing rapid decrease of T_N to 0 for $x = 0.1$ and weak decrease of T_{MI} from ~ 360 to ~ 340 K for $x = 0.2$. Dissimilar to hole doping by oxygen, hole doping in $\text{Nd}_{1-x}\text{Ca}_x\text{BaCo}_2\text{O}_{5.5}$ induces a systematic increase of resistivity and an increase of T_C up to 340 K, the highest observed for these cobaltites.

II. SYNTHESIS AND EXPERIMENTAL TECHNIQUES

Polycrystalline $\text{Nd}_{1-x}\text{Ca}_x\text{BaCo}_2\text{O}_{5.5}$ samples in the $0.0 \leq x \leq 0.2$ range were synthesized by the solid state reaction of appropriate amounts of Nd_2O_3 (dried in air), Co_3O_4 , CaCO_3 , and BaCO_3 (all $>99.99\%$ purity). Reactants were thoroughly mixed in an agate mortar and fired in air several times in the 900°C – 1150°C range, with intermediate grindings. The reaction was monitored with x-ray diffraction measurements, performed after each step of the synthesis procedure using a Rigaku D/MAX powder diffractometer in the 20° – 70° range with $\text{CuK}\alpha$ radiation. After achieving single-phase samples, the final step of the synthesis procedure was balancing the oxygen content by annealing in ultrapure argon gas at 390°C for 3 days. Partial pressure of oxygen was kept at less than 20 ppm. After firing in argon gas at 390°C , our samples were cooled to room temperature by turning off the furnace (natural furnace cooling at $\sim 3^\circ/\text{min}$ at 300°C and a slower rate at lower temperatures).

Thermogravimetric analysis (TGA) was performed on a Cahn TG171 thermobalance in several flowing gas mixtures up to 1100°C to determine the oxygen stoichiometry as a function of oxygen pressure and temperature and to determine the exact oxygen content of the final samples. The weight of the ~ 1 -g samples was measured with $5\text{-}\mu\text{g}$ precision. Oxygen content in the samples was determined by the weight difference between the initial sample and the total reduction products Nd_2O_3 , BaO , CaO , and metallic Co obtained by slow reduction in 42% hydrogen/argon atmosphere ($1^\circ/\text{min}$) up to the point of no weight change. Typical TGA results are presented in Fig. 1. Fig. 1(a) shows heating and cooling data in pure oxygen for a starting sample $\text{Nd}_{0.94}\text{Ca}_{0.06}\text{BaCo}_2\text{O}_{5.51 \pm 0.01}$, obtained from annealing in ultrapure argon gas at 360°C for 3 days. On heating, the sample absorbs oxygen at relatively low temperatures of 200°C – 300°C . Further heating to higher temperatures of 500°C results in the release of some oxygen, which is readily reabsorbed on cooling, indicating fast surface and bulk oxygen exchange at these temperatures. Cooling to room temperature results in final oxygen content of 5.78. Subsequent heating in Ar results in fast release of oxygen, with a characteristic narrow plateau near 390°C , which indicates the presence of an enhanced stability of oxygen composition at 5.50. Similar experiments were conducted to determine the annealing conditions necessary for obtaining samples with stoichiometric oxygen content 5.50. The total oxygen content of all samples

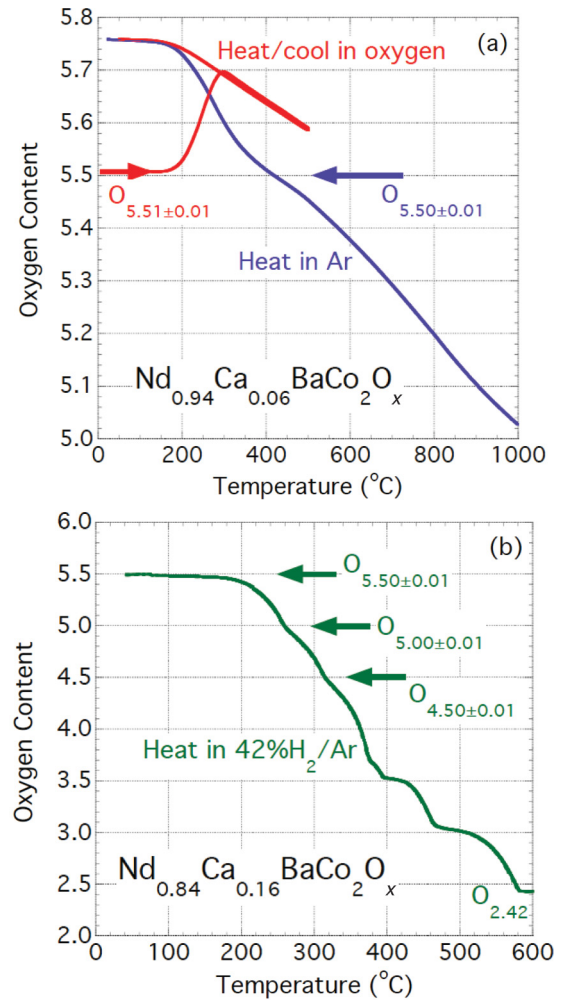


FIG. 1. (Color online) Oxygen content as a function of temperature for (a) $\text{Nd}_{0.94}\text{Ca}_{0.06}\text{BaCo}_2\text{O}_{5.51 \pm 0.01}$ during heating/cooling in oxygen and heating in Ar and (b) stoichiometric $\text{Nd}_{0.84}\text{Ca}_{0.16}\text{BaCo}_2\text{O}_{5.50 \pm 0.01}$ during heating in 42% H_2/Ar (note the enhanced stability of oxygen composition at 5.00 and 4.50).

was determined by slow reduction in 42% hydrogen/argon atmosphere, an example of which is shown in Fig. 1(b) for the starting sample $\text{Nd}_{0.84}\text{Ca}_{0.16}\text{BaCo}_2\text{O}_{5.50 \pm 0.01}$, obtained from annealing in ultrapure argon gas at 390°C for 3 days. The oxygen content of the remaining $\text{Nd}_{1-x}\text{Ca}_x\text{BaCo}_2\text{O}_{5.5}$ samples was confirmed to be 5.50 within the experimental error of ~ 0.01 . Overall starting and final cation compositions have been confirmed by energy dispersive x-ray spectroscopy on a Hitachi S-4700 electron microscope at the Electron Microscopy Center or Argonne National Laboratory.

Neutron powder diffraction experiments were performed at room temperature at the Oak Ridge National Laboratory Spallation Neutron Source ($0 \leq x \leq 0.16$) and at the Australian Bragg Institute ($x = 0.18, 0.20$). Time-of-flight data were collected at the high-resolution diffractometer (POWGEN),²² whereas a constant wavelength of 2.4395 \AA was selected for the $x = 0.18$ and 0.20 experiments (using the diffractometer Echidna). Structural refinements were performed by the Rietveld method with the GSAS/EXPGUI suite of programs.²³ In all refinements, the background was modeled using a shifted Chebyshev polynomial with 16 refinable parameters.

For Echidna, the profile function was modeled using the modified Thomson-Cox-Hasting pseudo-Voigt function with anisotropic broadening. For POWGEN, Von Dreele's exponential pseudo-Voigt convolution profile function was used. Significant deviations of the refined structural parameters (not shown in further analysis) for $x = 0.20$ suggested that the solubility limit was reached for that composition.

The direct current magnetization was measured using a magnetic property measurement system (model MPMS-7, Quantum Design). The temperature dependence of magnetization was measured in the temperature range 5–600 K on cooling in a magnetic field of 1 kOe. From that, the Curie temperature, the Néel temperature, and the properties of the PM state were determined. Isothermal magnetization hysteresis loops were measured at several temperatures in magnetic fields up to 70 kOe. Electrical resistivity, thermal conductivity, and the Seebeck coefficient were all measured using a physical property measurement system (model 6000, Quantum Design).

III. RESULTS AND DISCUSSION

A. Crystal structure

At room temperature, the nuclear structure of the nonsubstituted parent material $\text{NdBaCo}_2\text{O}_{5.5}$ has widely been described as crystallizing in the orthorhombic $Pmmm$ space group with unit cell dimensions on the order of $a_p \times 2a_p \times 2a_p$, where a_p is the lattice parameter of a simple ABO_3 perovskite structure. Doubling of the b axis arises from the alternation of ordered octahedral and pyramidal cobalt sheets. The pyramidal layers form by corner-shared coupling of oppositely oriented pairs of cobalt pyramids. In turn, the pyramidal pairs promote the ordering of Nd and Ba on independent and alternating layers, thus doubling the c axis as well. In the Ba layers, oxygen atoms fully occupy their crystallographic sites, whereas significant vacancies and oxygen/vacancy ordering take place in the Nd layers. However, the remaining perfectly ordered oxygen atoms O3 serve as apices for the corner-sharing CoO_6 octahedra.

At low temperature, $\text{RBaCo}_2\text{O}_{5.5}$ materials exhibit ferrimagnetic properties, as suggested by the unexpected weak ferrimagnetic signal. From a structural point of view, ferrimagnetism would be expected when two ferrimagnetic sublattices (of different magnitudes) would AFM couple along a particular direction. A weak ferrimagnetic signal could also arise from the cooperative canting of AFM-ordered magnetic moments. For $\text{RBaCo}_2\text{O}_{5.5}$, the low-temperature magnetic structures have all been associated with the appearance of superstructure peaks that require doubling of the a axis to form a superlattice with the dimensions $2a_p \times 2a_p \times 2a_p$ ¹² (Fig. 2). In this work, we were successful in driving the magnetic transition to temperatures at or above 300 K by simple chemical substitution of Ca at the Nd sites. While there is general agreement concerning the size of the superstructure unit cell, the magnetic structures and corresponding space group symmetries remain debatable. However, determining the exact magnetic symmetry for our Ca-substituted samples is not attempted in the present work, because our neutron data collected at room temperature only contain weak magnetic peaks. Plans to collect neutron data at low and high temperatures are being pursued.

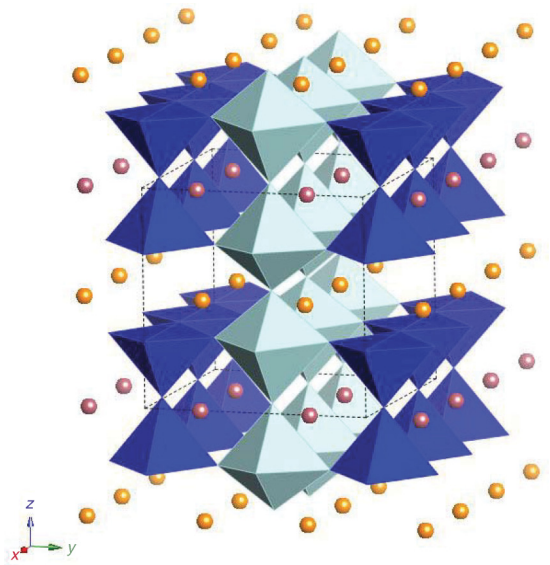


FIG. 2. (Color online) Crystal structure of $\text{Nd}_{1-x}\text{Ca}_x\text{BaCo}_2\text{O}_{5.5}$.

We now summarize our current understanding of the structure of $\text{RBaCo}_2\text{O}_{5.5}$. First, the $2a_p \times 2a_p \times 2a_p$ superstructure must be a subgroup of the parent $Pmmm$ structure, induced by subtle distortions associated with Ca substitution, long-range ordering of the Co magnetic moments, or both. Eight subgroup models consistent with doubling of the a axis (k-point x) is possible using the symmetry operators of space groups $Pmmm$, $Pmma$, $Pmam$, and $Pmaa$. $Pmam$ is essentially the same as $Pmma$, but the permutation of the symmetry elements allows the splitting of different atoms on independent sites. The four space groups allow structural models with the origin located at $(0, 0, 0)$ or shifted to $(1/2, 1/2, 0)$. Each of these eight models allows distinct displacive modes, but of particular interest to this work is the difference in the number of independent cobalt, Nd(Ca) and Ba, and/or oxygen sites. Satisfactory agreement factors were obtained using the published $Pmma$ model ($Pmma$ -1), in addition to two other models: $Pmma$ -2, with its origin shifted to match that of the parent $Pmmm$ structure, and $Pmaa$.

Relying on single crystal x-ray diffraction and group theory considerations, Chernyshov *et al.*²⁴ proposed a model based on the $Pmma$ symmetry in which the origin of the unit cell was shifted to $(1/2, 1/2, 0)$ with respect to $Pmmm$ to split the cobalt ions into four independent sites (two octahedral and two pyramidal sites). With this choice, the cobalt ions are allowed to have four independent magnetic moments of different magnitudes and orientations, which may explain the observed weak magnetic signal. Additional splitting of the oxygen atoms is also required. Our refinements using this model were difficult to converge without the introduction of extensive structural constraints and severe damping of all refined variables. Plots of the internal bond lengths and bond angles as a function of increased calcium content unveiled the erratic behavior of severe structural distortions from which no physical trends could be extracted.

Shifting the origin back to that of $Pmmm$ ($Pmma$ -2) or using the new space group $Pmaa$ reduces the number of independent Co sites to only two. In $Pmma$ -2, splitting of two oxygen sites

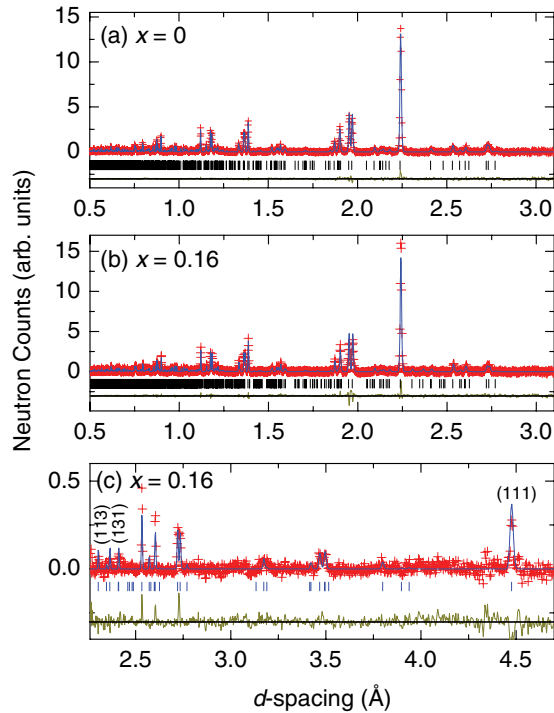


FIG. 3. (Color online) Results of Rietveld analysis of neutron time-of-flight data for (a) $\text{NdBaCo}_2\text{O}_{5.5}$ and (b) and (c) $\text{Nd}_{0.84}\text{Ca}_{0.16}\text{BaCo}_2\text{O}_{5.5}$ at room temperature.

would be required, whereas in *Pmaa*, the splitting of only one oxygen site was needed and the refinements converged immediately without any constraints or damping. However, all three models produced similar agreement factors and best-fit Rietveld plots. Plots shown in Fig. 3 were obtained using the *Pmaa* model. However, the magnetic structure refined in all three models produce a perfectly aligned G-type AFM sublattice that is not capable of explaining any ferrimagnetism. At room temperature, the observed ferrimagnetic signals of $\sim 0.1\text{--}0.2 \mu_B$ are significantly below the typical neutron detection limit of $\sim 0.3\text{--}0.5 \mu_B$.

As described previously, the agreement factors alone cannot be used to discriminate against one model or another; however, the smoothly varying internal bond lengths and bond angles obtained with the *Pmaa* candidate lead us to choose this space group as suitable for describing the nuclear symmetry. The magnetic symmetry, which is not necessarily the same as the nuclear symmetry, will be dealt with after collecting low-temperature data with significant magnetic intensities. However, for this work, the weak magnetic intensities were fit using the symmetry of the magnetic space group *Pmaa'*. Removing the time reversal symmetry of the second *a*-glide allows the construction of a G-type AFM structure in which two distinct magnetic moments for Co1 and Co2 can be refined. The magnetic moments lie parallel to the *a* axis with no canting allowed by symmetry in any other direction. Each spin (e.g., for Co1) is AFM coupled with six (four Co1 and two Co2) nearest-neighboring spins. Likewise, each Co2 spin is AFM coupled with four Co2 and two Co1 spins. The refined magnetic moments M_x are shown in Fig. 4(c) and listed in Table II for $0.08 \leq x \leq 0.18$ (i.e., samples with discernible magnetic peaks at room temperature). Representative best-fit

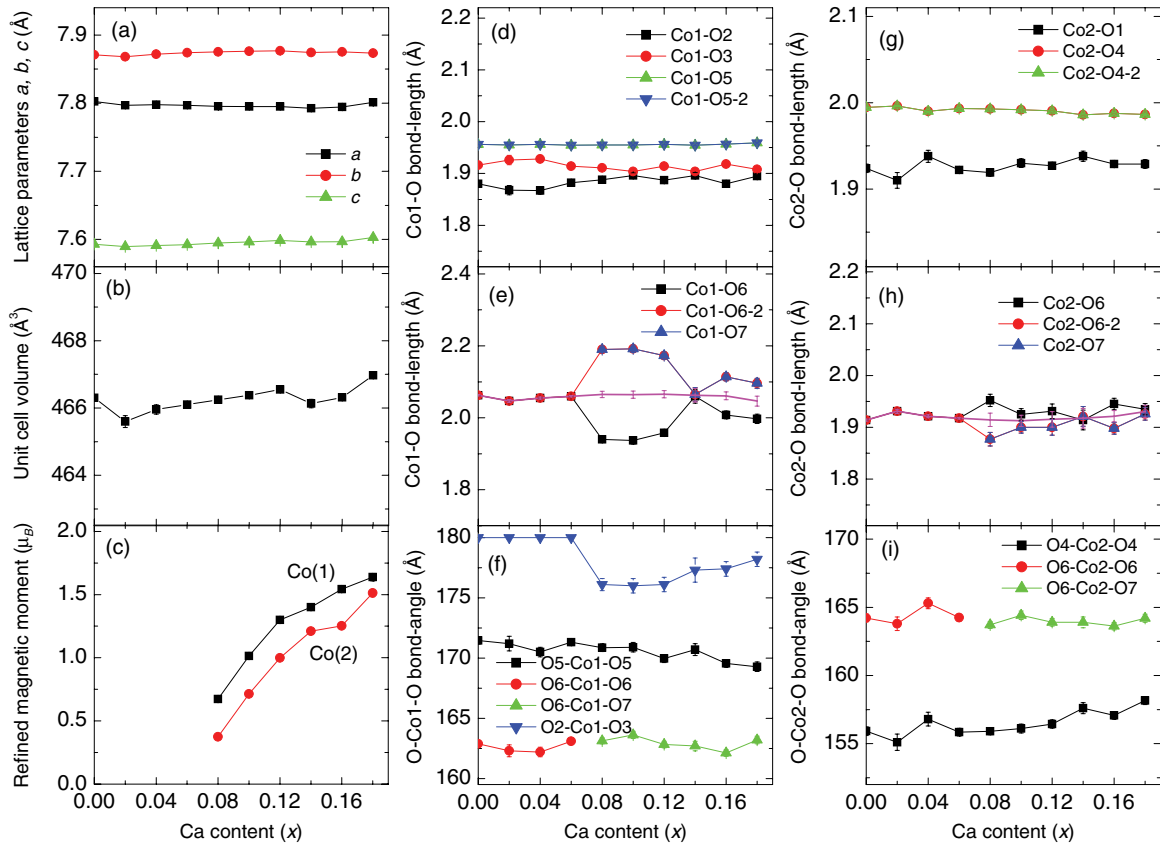
Rietveld refinements are presented in Fig. 3 for the $x = 0$ and 0.16 samples.

The structural results presented in Tables I and II were obtained with the assumption that the oxygen sublattice ($\text{O}_{5.5}$) is perfectly ordered. Because some degree of oxygen disorder is to be realistically expected, as discussed in Refs. 25–27, we investigated the possibility that the site of the O3 octahedral apices may not be fully occupied and that the otherwise “missing” oxygen would partly occupy the available vacancy sites within the pyramidal sheets. This situation would depict some degree of disorder in the otherwise perfectly ordered network of octahedral and pyramidal cobalt. For all samples, the fractional occupancy of O3 refined to within the range 0.90–0.99 (± 0.03), essentially indicating full site occupancy within one to three standard deviations, which is in good agreement with the TGA hydrogen reduction results described and shown in the previous section. No extra oxygen was found, as expected for perfectly oxygen-ordered materials, in any quantity at the vacant sites between the pyramids. All remaining main frame oxygen atoms refined to full occupancy within one or two standard deviations on their respective sites (i.e., O1, O2, O4–O6, and when present, O7); therefore, they were kept fixed during the final refinements. We conclude that our samples exhibit perfect long-range oxygen ordering, consistent with the alternating pyramidal and octahedral structural sheets shown in Fig. 2.

As shown in Fig. 4, the substitution of Nd^{3+} (10 coordinated) by the slightly larger Ca^{2+} ions results in a negligible effect on the lattice parameters and unit cell volume. This unexpected result may be explained by the opposite effects on the lattice generated by the increase of the valence of Co cations above $3+$ (i.e., by the formation of smaller Co^{4+} ions). At $x = 0.18$, the average Co oxidation state would be 3.09, indicating that only slight hole doping takes place by calcium substitution in the $0 \leq x \leq 0.18$ range. Therefore, it is difficult to obtain systematic trends in the behavior of the Co–O bond lengths as a function of increasing Ca content. Nonetheless, these bonds remain flat on average, with a slight trend toward shorter average values for higher Ca concentrations. For the magnetic $x \geq 0.08$ samples, we note an abrupt change in the Co–O bond lengths connecting the Co pyramids to the Co octahedra (i.e., Co–O6 and Co–O7). At the same time, the initially 180° apical O2–Co1–O3 bond angle buckles by a few degrees, seemingly in response to the long-range ordering of the cobalt magnetic moment. The local environment around the pyramidal cobalt ions remains largely unaffected. Our data suggest that hole-doping primarily takes place at the octahedral Co1 sites. Evolution of the refined Co1 and Co2 magnetic moments is shown in Fig. 4. Tables I and II list the most relevant crystallographic information and the corresponding bond lengths and bond angles for the whole series.

B. Electrical and thermal transport properties

Temperature dependences of the Seebeck coefficient α , the electrical resistivity ρ , and thermal conductivity κ are presented in Fig. 5. The Seebeck coefficient at temperatures below T_{MI} (100–300 K) is large and positive, which points at a slightly hole-overdoped state for all compositions in the entire Ca substitution range. This observation is in agreement


 FIG. 4. (Color online) Refined structural parameters for $\text{Nd}_{1-x}\text{Ca}_x\text{BaCo}_2\text{O}_{5.5}$ as a function of Ca content.

with the results of the TGA analysis and diffraction data. The low-temperature Seebeck coefficient decreases with x , similar to hole doping by oxygen in single crystals of $\text{GdBaCo}_2\text{O}_{5+\delta}$.⁶ At these temperatures, the resistivity is semiconducting and roughly increases with an increase in Ca content. This trend is opposite to the observed decrease of resistivity upon hole doping within the same doping range in $\text{GdBaCo}_2\text{O}_{5+\delta}$.⁶ In the latter case, the resistivity decreases with increasing δ and eventually becomes metallic in character for $\delta > 0.7$. The difference may arise from structural causes, such as a more conducting three-dimensional Co-O network with a larger amount of CoO_6 octahedra for $\delta > 0.5$. In addition, our resistivity values are considerably larger than measured for single crystals of $\text{GdBaCo}_2\text{O}_{5+\delta}$ with the difference increasing at decreasing temperatures, indicating considerable contribution of grain boundary scattering resistivity in polycrystalline samples. The combination of the measured transport properties gives the thermoelectric figure of merit $ZT = \alpha^2 T / \kappa \rho \sim 0.02$, which attains maximum values close to room temperature for low Ca content (0.04–0.10). Taking into account decreased electrical conductivity in our polycrystalline samples, these ZT s should be considered the lower estimates of achievable values.

At the MIT temperature T_{MI} , a characteristic drop in resistivity is observed. The resistivity values (10^{-2} – $10^{-3} \Omega\text{cm}$) right above T_{MI} are lower by more than an order of magnitude than those below T_{MI} , although the temperature dependence is not strictly metallic. Nevertheless, we use the term MIT to describe this transition in layered cobaltites. A hysteresis of a few degrees in resistivity can be observed at T_{MI} for

the family of $\text{Nd}_{1-x}\text{Ca}_x\text{BaCo}_2\text{O}_{5.5}$ samples, confirming first order transition. The resistivity above T_{MI} also increases with increasing x (it decreases with increasing δ in $\text{GdBaCo}_2\text{O}_{5+\delta}$ single crystals). At the same characteristic temperature, a pronounced drop in the Seebeck coefficient and a significant jump in thermal conductivity κ are observed, which point to correlated changes of the electronic and thermal transport at T_{MI} . In Fig. 5(c), we present the electronic part of the thermal conductivity, calculated according to the Wiedemann-Franz relationship $\kappa_E = L_0 \sigma T$, where $L_0 = 2.45 \cdot 10^{-8} \text{ W } \Omega / \text{K}^2$ is the Lorenz number and σ is the electrical conductivity. The electronic thermal conductivity is small compared to the lattice thermal conductivity below T_{MI} but increases significantly above T_{MI} . The magnitudes of the change in electronic and lattice thermal conductivities across T_{MI} are comparable, which underscores the coupling between the thermal and the electronic properties at the transition. For $x = 0$, the size of the jump of the electronic part of the thermal conductivity is $\sim 0.5 \text{ W/Km}$. The drop of the Seebeck coefficient and a change of its sign above T_{MI} in pure $\text{RBaCo}_2\text{O}_{5.5}$ has been interpreted as a spin blockade effect.²⁸

In Fig. 6(a), the Seebeck coefficient α at several temperatures is plotted as a function the Ca concentration x , which is nominally twice the amount of hole doping per Co. A decrease of α with Ca doping is similar to a decrease of α with increased oxygen content in $\text{RBaCo}_2\text{O}_{5.5+\delta}$ (full circles indicate data taken from Ref. 6). In the latter case, one oxygen ion per formula unit introduces two holes, so the Ca substitution and doping levels are related by $x = \delta/2$. The large and positive

TABLE I. Refined structural parameters for $\text{Nd}_{1-x}\text{Ca}_x\text{BaCo}_2\text{O}_{5.5}$, $0 \leq x \leq 0.06$ (at room temperature). Space group $Pmmm$: Nd/Ca $2p$, Ba $2o$, Co1 (octahedral, or oct, coordination) $2r$, Co2 (square pyramidal, or pyr, coordination) $2q$, O1 $1a$, O2 $1e$, O3 $1g$, O4 $2s$, O5 $2t$, and O6 $4u$. Isotropic temperature factors U_{iso} are multiplied by 100.

Ca content (x)		0	0.02	0.04	0.06
a	(Å)	3.90123(2)	3.8985(5)	3.8989(4)	3.8984(2)
b	(Å)	7.8709(5)	7.8681(10)	7.8719(8)	7.8739(4)
c	(Å)	7.5928(5)	7.5895(10)	7.5911(8)	7.5925(4)
Unit cell volume	(Å ³)	233.15(3)	232.80(5)	232.98(4)	233.05(2)
Nd/Ca	y	0.2721(2)	0.2724(4)	0.2725(3)	0.2715(2)
	U_{iso} (Å ²)	0.36(3)	0.52(5)	0.33(4)	0.42(3)
Ba	y	0.2502(3)	0.2502(7)	0.2506(5)	0.2507(3)
	U_{iso} (Å ²)	0.42(4)	0.73(9)	0.73(7)	0.40(4)
Co1 oct	y	0.5	0.5	0.5	0.5
	z	0.2476(6)	0.2462(12)	0.2460(9)	0.2479(6)
	U_{iso} (Å ²)	0.38(6)	0.5(1)	0.5(1)	0.38(6)
Co2 pyr	y	0	0	0	0
	z	0.2534(6)	0.2517(11)	0.2553(9)	0.2531(5)
	U_{iso} (Å ²)	0.34(6)	0.30(10)	0.36(9)	0.22(5)
O1	U_{iso} (Å ²)	0.91(6)	1.3(1)	0.98(9)	0.98(6)
O2	U_{iso} (Å ²)	0.53(6)	0.57(10)	0.66(9)	0.66(6)
O3	U_{iso} (Å ²)	0.38(5)	0.44(10)	0.51(8)	0.43(5)
O4	z	0.3082(4)	0.3084(7)	0.3081(5)	0.3081(3)
	U_{iso} (Å ²)	1.34(6)	1.55(11)	1.48(8)	1.34(5)
O5	z	0.2668(3)	0.2660(6)	0.2673(5)	0.2674(3)
	U_{iso} (Å ²)	0.72(4)	0.92(8)	1.03(7)	0.78(4)
O6	y	0.2409(3)	0.2430(4)	0.2421(3)	0.2412(2)
	z	0.2880(2)	0.2876(4)	0.2878(3)	0.2878(2)
	U_{iso} (Å ²)	0.90(3)	0.93(6)	0.93(5)	0.88(3)
Co1-O2	(Å)	1.880(5)	1.868(9)	1.867(7)	1.882(4)
Co1-O3	(Å)	1.916(5)	1.926(9)	1.928(7)	1.914(4)
Co1-O5 \times 2	(Å)	1.9561(4)	1.9551(8)	1.9562(6)	1.9548(4)
Co1-O6 \times 2	(Å)	2.063(2)	2.047(4)	2.055(3)	2.060(2)
Co2-O1	(Å)	1.924(5)	1.91(1)	1.938(7)	1.922(4)
Co2-O4 \times 2	(Å)	1.995(1)	1.996(2)	1.990(2)	1.993(1)
Co2-O6 \times 2	(Å)	1.914(2)	1.931(4)	1.921(3)	1.918(2)
O2-Co1-O3	(deg)	180	180	180	180
O5-Co1-Co5	(deg)	171.5(3)	171.2(6)	170.5(4)	171.3(3)
O6-Co1-Co6	(deg)	162.9(3)	162.3(5)	162.2(4)	163.1(3)
O4-Co2-O4	(deg)	155.9(3)	155.1(6)	156.8(5)	155.8(3)
O6-Co2-O6	(deg)	164.2(3)	163.8(5)	165.3(4)	164.2(3)
R_{wp} (%)		2.86	2.35	2.17	2.17
R_p (%)		3.93	5.31	3.35	3.74
χ^2		1.929	1.864	2.01	2.426

α at $T = 100\text{--}300$ K ($< T_{MI}$) becomes small above T_{MI} and shows a change of sign only for small x [Fig. 6(b)]. If a simple Coulomb blockade picture was adopted, in which the negative α is related to the hopping of electrons from Co^{2+} , created by charge disproportionation of Co^{3+} , we should observe that above $\sim x = 0.06$, the low values of α in the “metallic” state are positive, which would indicate that the increased concentration of delocalized Co^{4+} holes dominates the electrical transport above T_{MI} . The electrical resistivity of $\text{Nd}_{1-x}\text{Ca}_x\text{BaCo}_2\text{O}_{5.5}$ [Fig. 6(c)] is a complicated function of hole doping. In general, it increases with x , but this increase is nonmonotonic; at low temperatures of ~ 100 K, the resistivity demonstrates thermally activated behavior $\rho(T) = \exp(E_g/k_B T)$, where E_g is the activation energy and k_B is the Boltzmann constant. The determined values of E_g are presented in Fig. 6(d).

In further analysis, we attempted to follow the approach by Jonker²⁹ applied to $\text{RBaCo}_2\text{O}_{5.5}$ below⁶ and above⁷ T_{MI} , as well as to other mixed conductors.³⁰ That approach describes systems in which two-carrier (hole and electron) transport is present. For $\text{RBaCo}_2\text{O}_{5.5}$ material on the boundary between these two conduction mechanisms, this approach should be suitable. The balance between hole and electron conductivities determines a relation between the Seebeck coefficient α and the electrical conductivity σ . This relation in the Jonker approach is described as a universal pear-shaped curve, which in the extrinsic regime (for high conductivities) predicts a linear relation $\alpha = (k_B/e)\ln\sigma$. This relation was observed in Ref. 6 for $\text{RBaCo}_2\text{O}_{5+\delta}$. In the case of $\text{Nd}_{1-x}\text{Ca}_x\text{BaCo}_2\text{O}_{5.5}$, the relation between α and σ is anomalous (α and σ decrease simultaneously), which precludes the use of the Jonker model.

TABLE II. Refined structural parameters for $\text{Nd}_{1-x}\text{Ca}_x\text{BaCo}_2\text{O}_{5.5}$, $0.08 \leq x \leq 0.18$ (at room temperature). Space group $Pmaa$: Nd/Ca $4h$, Ba $4g$, Co1 (octahedral, or oct, coordination) $2f$, Co2 (square pyramidal, or pyr, coordination) $2e$, O1 $2e$, O2/O3 $2f$, O4 $4i$, O5 $4j$, and O6/O7 $4k$. Isotropic temperature factors U_{iso} are multiplied by 100.

Ca content		0.08	0.1	0.12	0.14	0.16	0.18
a	(Å)	7.79520(7)	7.79505(10)	7.79508(12)	7.7924(7)	7.79444(8)	7.80110(9)
b	(Å)	7.87538(8)	7.87608(11)	7.87672(13)	7.8745(7)	7.87535(9)	7.87333(9)
c	(Å)	7.59485(8)	7.59645(11)	7.59857(13)	7.5965(7)	7.59667(9)	7.60288(8)
Unit cell volume	(Å ³)	466.249(8)	466.380(11)	466.550(13)	466.13(7)	466.314(9)	466.974(9)
Nd/Ca	y	0.2709(2)	0.2701(2)	0.2691(2)	0.2671(3)	0.2676(2)	0.2653(5)
	U_{iso} (Å ²)	0.50(1)	0.48(2)	0.44(2)	0.52(4)	0.45(1)	0.43(5)
Ba	y	0.2511(3)	0.2505(4)	0.2498(3)	0.2512(5)	0.2502(4)	0.2484(7)
	U_{iso} (Å ²)	0.61(2)	0.57(4)	0.55(4)	0.67(6)	0.67(3)	0.68(7)
Co1 oct	y	0.492(1)	0.492(1)	0.492(1)	0.506(2)	0.499(2)	0.496(1)
	z	0.2485(6)	0.2495(7)	0.2482(6)	0.2495(8)	0.2475(6)	0.2492(6)
	U_{iso} (Å ²)	0.41(5)	0.33(7)	0.30(7)	0.33(11)	0.49(6)	−0.5(2)
	M_x (μ_B)	0.67(2)	1.01(2)	1.30(2)	1.44(2)	1.54(2)	1.64(2)
Co2 pyr	y	0.002(2)	0.006(1)	0.003(2)	0.005(2)	0.003(1)	0.002(1)
	z	0.2527(5)	0.2541(6)	0.2536(6)	0.2550(8)	0.2539(6)	0.2536(6)
	U_{iso} (Å ²)	0.24(4)	0.20(6)	0.29(6)	0.23(10)	0.07(4)	−0.7(2)
	M_x (μ_B)	0.37(2)	0.71(2)	1.00(2)	1.24(2)	1.25(2)	1.51(2)
O1	U_{iso} (Å ²)	0.95(4)	0.94(6)	0.87(5)	0.78(8)	0.74(4)	1.0(1)
O2	U_{iso} (Å ²)	0.86(4)	0.72(5)	0.67(5)	0.75(8)	0.62(3)	0.1(1)
O3	U_{iso} (Å ²)	0.54(4)	0.80(5)	1.12(6)	1.35(10)	1.23(5)	4.6(2)
O4	z	0.3074(3)	0.3080(4)	0.3070(3)	0.3054(5)	0.3054(3)	0.3031(4)
	U_{iso} (Å ²)	1.39(3)	1.40(5)	1.30(5)	1.26(7)	1.26(4)	1.59(9)
O5	z	0.2671(3)	0.2678(3)	0.2691(3)	0.2693(5)	0.2710(3)	0.2730(4)
	U_{iso} (Å ²)	1.03(3)	1.03(4)	0.99(4)	1.05(6)	1.14(3)	2.9(1)
O6	y	0.2482(4)	0.2482(5)	0.2460(6)	0.2465(9)	0.2481(5)	0.2454(8)
	z	0.2860(3)	0.2862(4)	0.2861(5)	0.286(1)	0.2862(3)	0.2884(4)
	U_{iso} (Å ²)	0.49(2)	0.53(4)	0.47(4)	0.7(1)	0.50(2)	0.63(9)
O7	y	0.2330(4)	0.2329(6)	0.2355(7)	0.2357(11)	0.2349(5)	0.2403(9)
	z	0.2906(4)	0.2901(6)	0.2916(7)	0.2945(11)	0.2932(4)	0.2887(5)
	U_{iso} (Å ²)	1.68(5)	1.45(7)	1.85(9)	1.6(2)	1.94(6)	3.6(1)
Co1-O2	(Å)	1.888(4)	1.896(5)	1.887(4)	1.896(6)	1.880(5)	1.895(5)
Co1-O3	(Å)	1.911(4)	1.904(5)	1.914(4)	1.904(6)	1.918(5)	1.908(5)
Co1-O5 × 2	(Å)	1.9550(4)	1.9549(5)	1.9563(5)	1.9545(7)	1.9567(5)	1.9589(5)
Co1-O6	(Å)	1.940(9)	1.94(1)	1.96(1)	2.06(2)	2.01(1)	1.997(12)
Co1-O7	(Å)	2.19(1)	2.19(1)	2.17(1)	2.07(2)	2.11(1)	2.10(1)
Co2-O1	(Å)	1.919(4)	1.930(5)	1.927(4)	1.938(6)	1.929(4)	1.929(5)
Co2-O4 × 2	(Å)	1.993(1)	1.992(1)	1.991(1)	1.986(2)	1.988(1)	1.986(1)
Co2-O6	(Å)	1.95(1)	1.93(1)	1.93(1)	1.91(2)	1.95(1)	1.94(1)
Co2-O7	(Å)	1.88(1)	1.90(1)	1.90(2)	1.92(2)	1.90(1)	1.93(1)
O2-Co1-O3	(deg)	176.1(5)	176(6)	176.1(6)	177.0(10)	177.4(6)	178.2(6)
O5-Co1-Co5	(deg)	170.9(3)	170.9(4)	170.0(3)	170.7(5)	169.6(3)	169.3(4)
O6-Co1-Co7	(deg)	163.1(3)	163.6(3)	162.8(3)	162.7(4)	162.1(3)	163.2(3)
O4-Co2-O4	(deg)	155.9(3)	156.1(3)	156.4(3)	157.6(4)	157.1(3)	158.2(3)
O6-Co2-O7	(deg)	163.7(3)	164.4(3)	163.9(3)	163.9(4)	163.6(3)	164.2(3)
R_{wp} (%)		2.57	2.75	3.38	3.08	3.48	4.71
R_p (%)		3.58	3.88	4.19	4.46	4.92	3.69
χ^2		2.034	1.983	2.323	2.394	2.838	1.634

The grain boundary carrier scattering in our polycrystalline materials is likely the main mechanism that hinders the intrinsic relation between the Seebeck coefficient and the electrical resistivity.

C. Magnetic properties

Temperature dependence of magnetization for $\text{Nd}_{1-x}\text{Ca}_x\text{BaCo}_2\text{O}_{5.5}$ that was measured on “field cooling” in a magnetic field of 1 kOe is presented in Fig. 7(a). A

small anomaly in the PM susceptibility can be observed at T_{MI} (see the Fig. 7 inset). This anomaly is associated with a spin state transition and is discussed later. The characteristic temperatures determined from the $M(T)$ dependences are presented in Fig. 7(b).

For the undoped ($x = 0$) material, the two transitions from PM to ferrimagnetic and from ferrimagnetic to AFM can be observed close to each other, manifesting as the presence of a narrow cusp around $T = 250$ K.

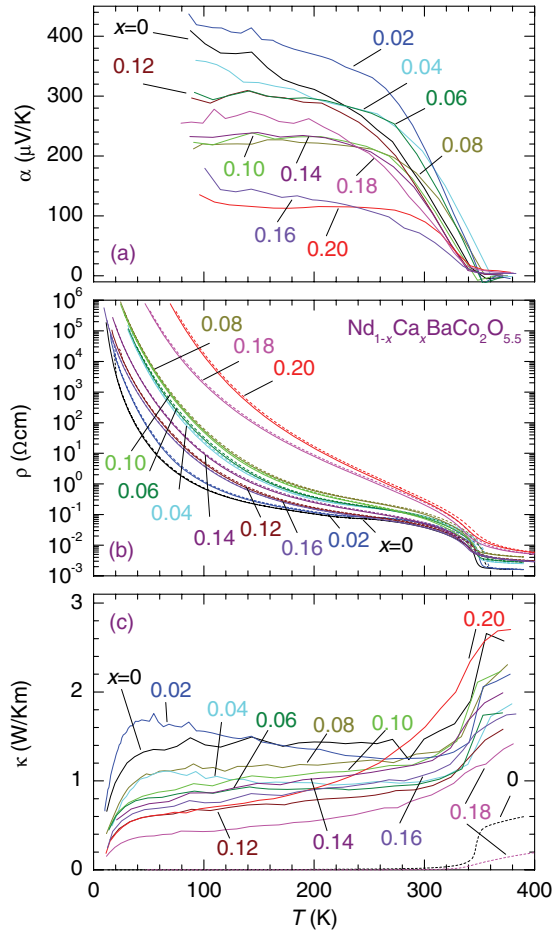


FIG. 5. (Color online) Temperature dependence of (a) the Seebeck coefficient, (b) electrical resistivity, and (c) thermal conductivity for $\text{Nd}_{1-x}\text{Ca}_x\text{BaCo}_2\text{O}_{5.5}$. Dashed lines in (c) represent the electronic contribution to thermal conductivity.

Upon Ca doping, the PM/ferrimagnetic transition is increasing and approaches T_{MI} , which slightly decreases at the same time. The ferrimagnetic/AFM transition temperatures decrease in a more pronounced way and disappear for $x \geq 0.1$, above which all compositions become fully ferrimagnetic. A similar decrease of the ferrimagnetic/AFM transition temperature has been observed for $\text{YBa}_{1-x}\text{Ca}_x\text{Co}_2\text{O}_{5.5}$ ¹⁶ at equivalent substitution levels of x . Because the substitution of Ca for Ba is isovalent, it should not change the oxidation state of Co, indicating that the main mechanism for suppression of the ferrimagnetic/AFM transition in that case should be attributed to the local disorder on the Ba/Ca site, which may also induce oxygen disorder. Charge doping by oxygen addition in $\text{GdBaCo}_2\text{O}_{5.5+\delta}$ also leads to suppression of the AFM phase; however, the ferrimagnetic/AFM transition temperature is suppressed only slightly before the oxygen defect-induced disorder at $\delta \sim 0.05$ leads to compositional phase separation. It is possible that the similar disorder-induced processes contribute to the suppression of the AFM state for our $\text{Nd}_{1-x}\text{Ca}_x\text{BaCo}_2\text{O}_{5.5}$ materials. However, this picture needs further clarification with respect to careful study of the samples total and local oxygen stoichiometry, as well as the presence of antisite defects on Ba and Nd sites for Ca-substituted materials.

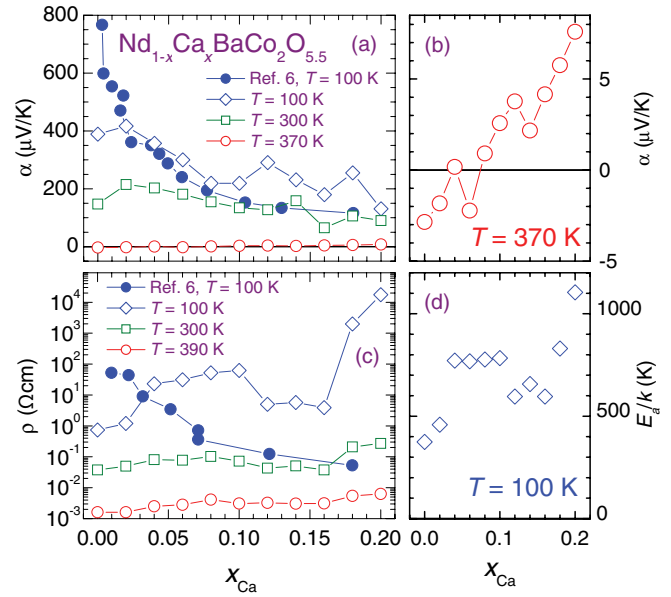


FIG. 6. (Color online) (a) The Seebeck coefficient below and above T_{MI} as a function of doping level (Ca concentration) in $\text{Nd}_{1-x}\text{Ca}_x\text{BaCo}_2\text{O}_{5.5}$. (b) The Seebeck coefficient at $T = 370$ K. (c) The electrical resistivity below and above T_{MI} . (d) Activation energy as a function of Ca concentration. Full circles in (a) and (c) are plotted after Ref. 6 (see the text).

In contrast to our samples, $\text{YBa}_{1-x}\text{Ca}_x\text{Co}_2\text{O}_{5.5}$ does not demonstrate an increase in T_C up to $x = 0.1$. This is similar to oxygen addition in $\text{GdBaCo}_2\text{O}_{5.5+\delta}$, where despite the equivalent charge doping to our materials, the local oxygen disorder causes a decrease of T_C . The increase of T_C observed for our samples is therefore associated with hole doping by Ca^{2+} for Nd^{3+} and creation of localized Co^{4+} ions. We argue that an alternative path to hole doping by oxygen defects introduces not only Co^{4+} ions but also disorder into the Co-O network by the formation of a larger amount of CoO_6 octahedra at the expense of CoO_5 pyramids. This effect causes increasing delocalization of electrons across Co-O-Co bonds and lowering T_C .

The molar magnetic susceptibility $\chi = M/H$, in the PM region, was used to determine the effective PM moment μ_{eff} by fitting the Curie-Weiss formula $\chi = \chi_0 + (1/8)\mu_{\text{eff}}^2/(T - \Theta)$. In this formula, χ_0 is a temperature-independent susceptibility, $\mu_{\text{eff}} = g\sqrt{S(S+1)}$ is the spin-only effective PM moment ($g = 2$ is the gyromagnetic factor, and S is the effective spin), and Θ is the PM Curie-Weiss temperature. Before the analysis, the calculated PM contribution of Nd^{3+} ions was subtracted from the experimental data. We assume that Nd^{3+} ions in $\text{Nd}_{1-x}\text{Ca}_x\text{BaCo}_2\text{O}_{5.5}$ follow the Curie law $\chi_{\text{Nd}} = (1-x)(1/8)(\mu_{\text{eff}}^{\text{Nd}})^2/T$ with the value $\mu_{\text{eff}}^{\text{Nd}} = 3.5$.

The analysis of the Curie-Weiss behavior was performed separately for the two PM regions: below and above MIT. Different behavior of the parameters of the PM state below and above T_{MI} , commonly described as the change of slope of the inverse susceptibility at T_{MI} , is observed. The PM Curie-Weiss temperature Θ below T_{MI} is always positive and coincides with T_C with small deviations for larger x . This observation points to ferrimagnetic interactions between $\text{Co}^{3+/4+}$ ions. For

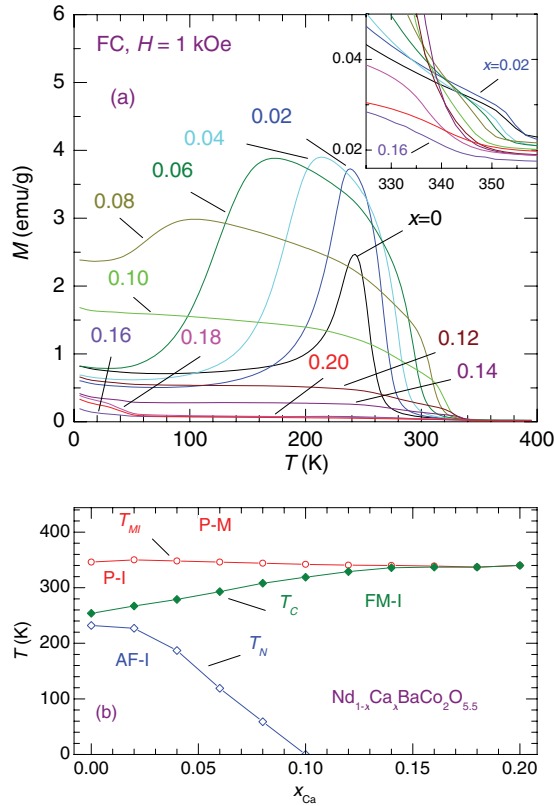


FIG. 7. (Color online) (a) Temperature dependence of magnetization for $\text{Nd}_{1-x}\text{Ca}_x\text{BaCo}_2\text{O}_{5.5}$ measured on field cooling (FC) in a magnetic field of 1 kOe. The inset shows the same data in the vicinity of T_{MI} . (b) Phase diagram in which P-M is the PM metallic phase, P-I is the PM insulating phase, FM-I is the ferrimagnetic insulating phase, and AF-I is the AFM insulating phase. The main transition temperatures T_{MI} , T_C , and T_N are plotted.

$T < T_{MI}$, χ_0 is negative (about -0.005 emu/mol), which is an indication of the presence of (diamagnetic) Co^{3+} ions that are in the LS state. For $T > T_{MI}$, the $M(T)$ dependences contain a significant PM temperature-independent background χ_0 ($1-4 \times 10^{-3}$ emu/mol, presumably of the Pauli type for these conductive materials) associated with an unknown fraction of Co ions. The effective PM moments for the remaining fraction (following the Curie-Weiss law) of Co ions above T_{MI} are generally larger ($5-7 \mu_B$), which is apparently associated with a transition of (some) Co^{3+} to higher spin states at T_{MI} . Θ is negative for most compounds, with a tendency to change the sign to positive values for larger x . The scattering of the μ_{eff} values hinders the unambiguous determination of the Co spin state above T_{MI} .

The lines in Fig. 8(b) show the $\mu_{\text{eff}}(x)$ dependences calculated for different spin states of Co^{3+} and Co^{4+} , according to the formula $\mu_{\text{eff}}^2(x) = (2-x)\mu_{\text{eff}}^2(\text{Co}^{3+}) + x\mu_{\text{eff}}^2(\text{Co}^{4+})$. (μ_{eff} is a PM moment for one formula unit, i.e., two cobalt ions.) Of all the simple models used, the best description of the observed $\mu_{\text{eff}}(x)$ dependence below T_{MI} is given by the model (Co3 IS/LS + Co4 LS), where Co^{3+} is in a combined spin state IS + LS in a 1:1 ratio (presumably one spin state for Co in the octahedra and one in the pyramids, but the magnetization measurements do not allow differentiation between these two sites) and Co^{4+} is the LS state. A possible disproportionation

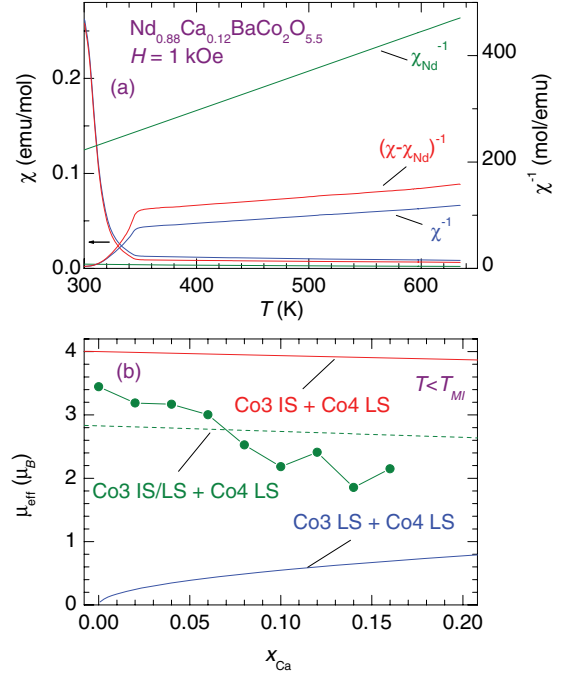


FIG. 8. (Color online) (a) The magnetic susceptibility of $\text{Nd}_{1-x}\text{Ca}_x\text{BaCo}_2\text{O}_{5.5}$ for $x = 0.12$. (b) The effective PM moments μ_{eff} below T_{MI} as a function of the Ca content (see the text). The lines denote several models for $\mu_{\text{eff}}(x)$ with different spin states for $\text{Co}^{4+/3+}$.

of Co^{3+} ions into Co^{2+} and Co^{4+} ^{7,28} does little to change the analysis, because the PM moment of a Co^{2+} :HS and Co^{4+} :LS pair ($4.24 \mu_B$) is only 6% higher than that of two Co^{3+} :IS ions.

Literature data for $\text{RBaCo}_2\text{O}_{5.5}$ support the LS state for octahedral cobalt in the insulating phase ($< T_{MI}$);^{3,6,31-33} however, there are also results suggesting the IS state³⁴ or HS state.^{35,36} For square pyramidal coordination, either the IS state^{3,6,31,32} or the HS state^{33,35,36} is proposed. The larger μ_{eff} above than below T_{MI} suggests that the fraction of Co^{3+} ions that are in the LS state below T_{MI} undergo a transition either to the IS or to the HS state.

Isothermal magnetization curves are presented in Fig. 9. In all samples, clear hysteresis and no saturation up to 70 kOe can be observed below T_C . This is also true for the AFM region, although the shape of the magnetization curves is different. More complicated magnetization curves can also be observed (not shown), which indicate competing AFM and ferrimagnetic interactions in these materials at low temperatures. For higher Ca concentrations, pronounced hysteresis can be observed at room temperature [Fig. 9(b)]. The parameters determined from $M(H)$ curves M_{70} (high field magnetization in $H = 70$ kOe) and M_{rem} (remanent magnetization in $H = 0$) are presented in Fig. 9(c).

Magnetization values M_{70} and M_{rem} in Fig. 9(d) are lower than expected for full saturation of magnetic Co^{3+} and Co^{4+} ions. For example, if we analyze the model, which describes best the Co spin states in the PM state below MIT—i.e., Co^{3+} in the mixture of LS ($S = 0$) + IS ($S = 1$) states and Co^{4+} ions in the LS ($S = 1/2$) state—the expected saturation magnetization is $M_s = 0(1 - 0.5x) + 2(1 - 0.5x) + x = 2 \mu_B$. All compositions present low values of M_{rem} . A significant increase of the magnetization can be observed for

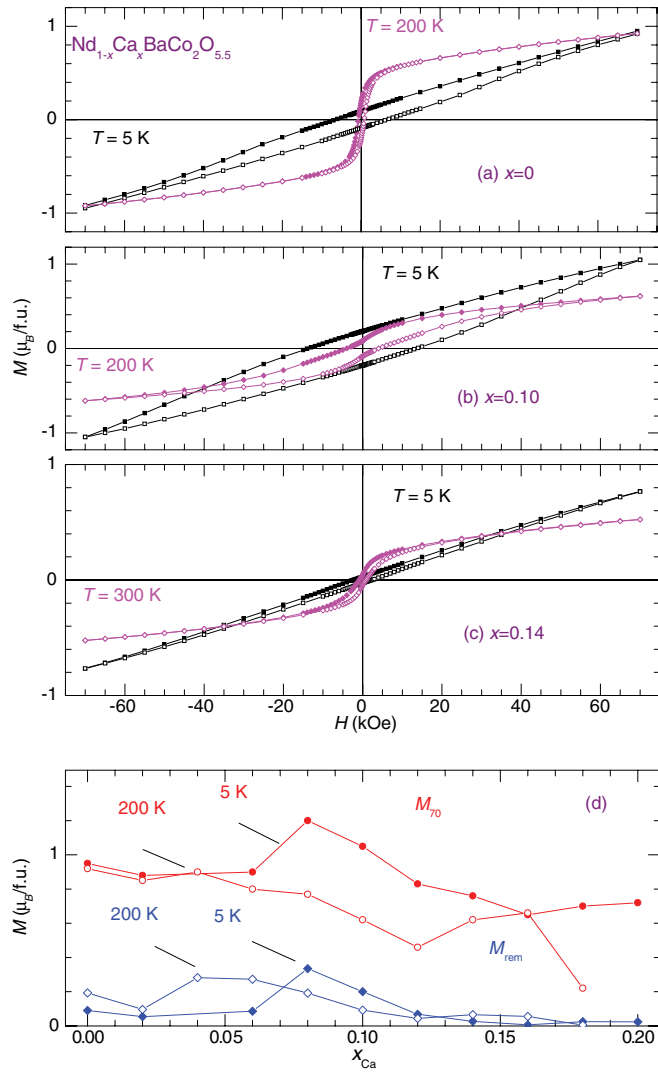


FIG. 9. (Color online) Magnetic hysteresis curves for (a) $x = 0$, (b) $x = 0.10$, and (c) $x = 0.14$ samples.

$x = 0.08$. This sample also demonstrates a large coercivity field $H_c \approx 13$ kOe at 5 K compared to other $\text{Nd}_{1-x}\text{Ca}_x\text{BaCo}_2\text{O}_{5.5}$ samples with $H_c = 2\text{--}5$ kOe.

IV. SUMMARY

We have synthesized and characterized a series of $\text{Nd}_{1-x}\text{Ca}_x\text{BaCo}_2\text{O}_{5.5}$ -layered cobaltites with cation and vacancy ordering in the range of $x = 0\text{--}0.2$. Hole doping by Ca substitution in this range preserves the MIT associated with an abrupt change of electrical and thermal transport properties and a Co^{3+} spin state transition. Our data indicate that half of Co^{3+} ions undergo a transition from the LS state to either the IS or the HS state on heating through T_{MI} . Upon Ca doping, the carriers involved in the transport above T_{MI} change from electrons to holes, showing that a simple Coulomb blockade model is not in effect. The low-temperature ferrimagnetic to AFM transition is suppressed above $x = 0.1$. The ferrimagnetic transition temperature is increasing with Ca doping to values close T_{MI} , which slightly decreases. This is the largest enhancement of ferrimagnetic properties observed for these cobaltites. Because there are two alternative methods to effectively charge dope $\text{RBaCo}_2\text{O}_{5.5+\delta}$ -layered cobaltites, it may be interesting to study $\text{Nd}_{1-x}\text{Ca}_x\text{BaCo}_2\text{O}_{5.5+\delta}$ materials as a function of oxygen doping for a fixed amount of substitution x to clarify the effects of disorder and doping on magnetic and electronic properties.

ACKNOWLEDGMENTS

Work at Northern Illinois University was supported by National Science Foundation Contract No. DMR-0706610. Work at Argonne National Laboratory was supported by the US Department of Energy, Office of Science, Office of Basic Energy Sciences under Contract No. DE-AC02-06CH11357. A portion of this research at Oak Ridge National Laboratory's Spallation Neutron Source was sponsored by the US Department of Energy, Office of Basic Energy Sciences, Scientific User Facilities Division.

*kolesnik@niu.edu

¹W. Zhou, *Chem. Mater.* **6**, 441 (1994).

²C. Martin, A. Maignan, D. Pelloquin, N. Nguyen, and B. Raveau, *Appl. Phys. Lett.* **71**, 1421 (1997).

³A. Maignan, C. Martin, D. Pelloquin, N. Nguyen, and B. Raveau, *J. Solid State Chem.* **142**, 247 (1999).

⁴D. Akahoshi and Y. Ueda, *J. Solid State Chem.* **156**, 355 (2001).

⁵E. Suard, F. Fauth, V. Caignaert, I. Mirebeau, and G. Baldinozzi, *Phys. Rev. B* **61**, R11871 (2000).

⁶A. A. Taskin, A. N. Lavrov, and Y. Ando, *Phys. Rev. B* **71**, 134414 (2005).

⁷A. Y. Suntssov, I. A. Leonidov, M. V. Patrakeev, and V. L. Kozhevnikov, *J. Solid State Chem.* **184**, 1951 (2011).

⁸F. Fauth, E. Suard, V. Caignaert, B. Domenges, I. Mirebeau, and L. Keller, *Eur. Phys. J. B* **21**, 163 (2001).

⁹T. Vogt, P. M. Woodward, P. Karen, B. A. Hunter, P. Henning, and A. R. Moodenbaugh, *Phys. Rev. Lett.* **84**, 2969 (2000).

¹⁰F. Fauth, E. Suard, V. Caignaert, and I. Mirebeau, *Phys. Rev. B* **66**, 184421 (2002).

¹¹Y. P. Chernenkov, V. P. Plakhty, V. I. Fedorov, S. N. Barilo, S. V. Shiryaev, and G. L. Bychkov, *Phys. Rev. B* **71**, 184105 (2005).

¹²V. P. Plakhty, Y. P. Chernenkov, S. N. Barilo, A. Podlesnyak, E. Pomjakushina, E. V. Moskvina, and S. V. Gavrilov, *Phys. Rev. B* **71**, 214407 (2005).

¹³Y. P. Chernenkov, V. P. Plakhty, A. G. Gukasov, S. N. Barilo, S. V. Shiryaev, G. L. Bychkov, V. Hinkov, V. I. Fedorov, and V. A. Chekanov, *Phys. Lett. A* **365**, 166 (2007).

¹⁴D. D. Khalyavin, *Phys. Rev. B* **72**, 134408 (2005).

¹⁵D. D. Khalyavin, D. N. Argyriou, U. Amann, A. A. Yaremchenko, and V. V. Kharton, *Phys. Rev. B* **75**, 134407 (2007).

¹⁶G. Aurelio, J. Curiale, R. D. Sanchez, and G. J. Cuello, *Phys. Rev. B* **76**, 214417 (2007).

¹⁷A. Bharathi, P. Yasodha, N. Gayathri, A. T. Satya, R. Nagendran, N. Thirumurugan, C. S. Sundar, and Y. Hariharan, *Phys. Rev. B* **77**, 085113 (2008).

- ¹⁸Y.-K. Tang and C. C. Almasan, *Phys. Rev. B* **77**, 094403 (2008).
- ¹⁹M. Motin Seikh, V. Caignaert, V. Pralong, and B. Raveau, *Solid State Comm.* **149**, 697 (2009).
- ²⁰M. Motin Seikh, V. Caignaert, V. Pralong, C. Simon, and B. Raveau, *J. Phys. Condens. Matter* **20**, 015212 (2008).
- ²¹M. Motin Seikh, B. Raveau, V. Caignaert, and V. Pralong, *J. Magn. Magn. Mater.* **320**, 2676 (2008).
- ²²A. Huq, J. P. Hodges, O. Gourdon, and L. Heroux, *Z. Kristallogr. Proc.* **1**, 127 (2011).
- ²³A. C. Larson and R. B. Von Dreele, General Structure Analysis System (GSAS), Los Alamos National Laboratory Report LAUR 86-748 (2004); B. H. Toby, *J. Appl. Cryst.* **34**, 210 (2001).
- ²⁴D. Chernyshov, V. Dmitriev, E. Pomjakushina, K. Conder, M. Stingaciu, V. Pomjakushin, A. Podlesnyak, A. A. Taskin, and Y. Ando, *Phys. Rev. B* **78**, 024105 (2008).
- ²⁵C. Frontera, J. L. García-Muñoz, O. Castaño, C. Ritter, and A. Caneiro, *J. Phys. Condens. Matter* **20**, 104228 (2008).
- ²⁶S. Streule, A. Podlesnyak, J. Mesot, M. Medarde, K. Conder, E. Pomjakushina, E. Mitberg, and V. Kozhevnikov, *J. Phys. Condens. Matter* **17**, 3317 (2005).
- ²⁷C. Frontera, J. L. García-Muñoz, and O. Castaño, *J. Appl. Phys.* **103**, 07F713 (2008).
- ²⁸A. Maignan, V. Caignaert, B. Raveau, D. Khomskii, and G. Sawatzky, *Phys. Rev. Lett.* **93**, 026401 (2004).
- ²⁹G. H. Jonker, Philips Res. Rep. **23**, 131 (1968); G. M. Choi, H. L. Tuller, and D. Goldschmidt, *Phys. Rev. B* **34**, 6972 (1986).
- ³⁰S. R. Sehlin, H. U. Anderson, and D. M. Sparlin, *Phys. Rev. B* **52**, 11681 (1995).
- ³¹M. Respaud, C. Frontera, J. L. García-Muñoz, M. A. G. Aranda, B. Raquet, J. M. Broto, H. Rakoto, M. Goiran, A. Llobet, and J. Rodriguez-Carvajal, *Phys. Rev. B* **64**, 214401 (2001).
- ³²C. Frontera, J. L. García-Muñoz, A. Llobet, and M. A. G. Aranda, *Phys. Rev. B* **65**, 180405 (2002).
- ³³J. F. Mitchell, J. Burley, and S. Short, *J. Appl. Phys.* **93**, 7364 (2003).
- ³⁴Y. Moritomo, T. Akimoto, M. Takeo, A. Machida, E. Nishibori, M. Takata, M. Sakata, K. Ohoyama, and A. Nakamura, *Phys. Rev. B* **61**, R13325 (2000).
- ³⁵H. Wu, *J. Phys. Condens. Matter* **15**, 503 (2003).
- ³⁶W. R. Flavell, A. G. Thomas, D. Tsoutsou, A. K. Mallick, M. North, E. A. Seddon, C. Cacho, A. E. R. Malins, S. Patel, R. L. Stockbauer, R. L. Kurtz, P. T. Sprunger, S. N. Barilo, S. V. Shiryayev, and G. L. Bychkov, *Phys. Rev. B* **70**, 224427 (2004).